ACS APPLIED NANO MATERIALS

www.acsanm.org

Article

2D Amorphous/Crystalline *a*-In_2O_3/In_2Se_3 Nanosheet Heterostructures with Improved Capability for H_2 and NO_2 Sensing

Valentina Paolucci, Jessica De Santis, Vittorio Ricci,* Luca Lozzi, and Carlo Cantalini

Cite This: *ACS Appl. Nano Mater.* 2023, 6, 6011−6023

Read Online

ACCESS | Metrics & More | Article Recommendations | Supporting Information

ABSTRACT: Spontaneous degradation of 2D transition-metal dichalcogenides/chalcogenides (TMDs/MCs) gas sensors in dry/wet air represents one of the most significant drawback of these interfaces, hampering the reproducibility of the baseline resistance and sensor's signal stability (i.e., sensor's creep). Herein, we report a simple protection strategy stimulating the formation of a self-assembled oxide (*a*-MO_x) over TMDs/MCs, which promotes effective passivation of the underlying surface and excellent gas sensing response. Liquid-phase-exfoliated few-layers 2D-In_2Se_3 have been annealed in air at 180 °C for 24 h to yield an *a*-In_2O_3/In_2Se_3 heterostructure comprising a self-assembled *a*-In_2O_3 amorphous skin (5−10 nm) over 2D-crystalline In_2Se_3 (5−30 nm). The isomorphic conversion of In_2Se_3 into *a*-In_2O_3 specifically enables the layered shape of the precursor 2D-In_2Se_3 to be preserved after annealing, therefore providing all the surface-to-volume advantages of 2D interfaces. The excellent baseline and sensor's signal reproducibility to H_2 (5−100 ppm) and NO_2 (400 ppb−1 ppm) after 1 year of delivery at 100 °C operating temperature demonstrated that the oxide skin effectively passivates the underlying 2D-In_2Se_3 from further oxidation. Significantly, the *a*-In_2O_3/In_2Se_3 heterostructure shows better H_2 sensing response with respect to 2D TMDs/MCs sensors, with experimental detection limits as low as 5 ppm H_2 and 400 ppb NO_2, with associated RR (R_a/R_g) = 2.1 to 100 ppm H_2 and RR (R_g/R_a) = 2.3 to 1 ppm NO_2 in dry air. A charge carrier mechanism between the *a*-In_2O_3/In_2Se_3 heterostructure and H_2, NO_2, and H_2O molecules is presented to discuss the humidity cross response to H_2 and NO_2. The passivation strategy here proposed can be extended to a large variety of TMDs/MCs, opening new perspectives for the effective exploitation of layered amorphous gas-sensing interfaces.

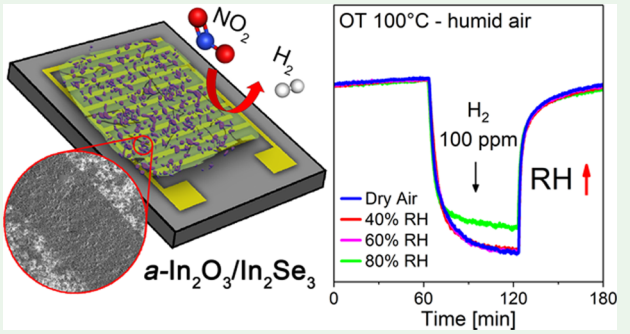

KEYWORDS: *a-In_2O_3/In_2Se_3 heterostructure, amorphous In_2O_3, (a-In_2O_3), chemoresistive, H_2 sensor, NO_2 sensor*

1. INTRODUCTION

Hydrogen as a clean and renewable fuel is one of the most promising energy carriers for the reduction of the environmental impact of the automotive and transport industry. Despite that, hydrogen-related hazards in production, storage, and transport (explosion range 4−75% vol H_2 in air) represent crucial issues for its safe exploitation, challenging new sensor platforms suitable to detect colorless and odorless hydrogen leaks, down to a few parts per million (ppm). Nitrogen dioxide, on the other hand, is a ubiquitous gas deriving from emissions from vehicles, power plants, and factories, mostly as a byproduct of the combustion process. EPA's standards for NO_2 limit people's short-term exposures to 100 ppb, making its actual measure challenging in complex urban and indoor gaseous atmospheres.[1]

Chemoresistive H_2 and NO_2 sensors based on different metal oxides (MO) have been recently reviewed,[2,3] highlighting the excellent H_2/NO_2 sensing properties of different sensor architectures at operating temperatures (OTs) in the range of 200−260 °C. More recently, new H_2/NO_2 gas platforms, based on few layers of exfoliated van der Waals (vdW) transition-metal dichalcogenides (TMDs) and metal chalcogenides (MCs), operating at lower temperatures (i.e., 25−100 °C), have been investigated as possible alternatives to traditional H_2/NO_2 MO sensors.[4] These TMDs/MCs nanosheet interfaces, which can be easily engineered into complex 0D−1D−3D architectures[5] and 2D/2D heterostructures,[6−8] provide all the surface-to-volume advantages of layered interfaces, enabling the transduction of sub-ppm concentrations of NO_2 and ppm level of less electronegative gases like H_2 and CO.

Remarkably, few layers of exfoliated TMDs and MCs chemoresistive sensors are subjected to fast oxidation/degradation in dry/humid laboratory conditions.[9] Their thermodynamic instability, demonstrated by the spontaneous

Received: January 26, 2023
Accepted: March 9, 2023
Published: April 3, 2023

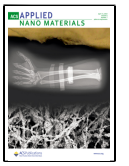

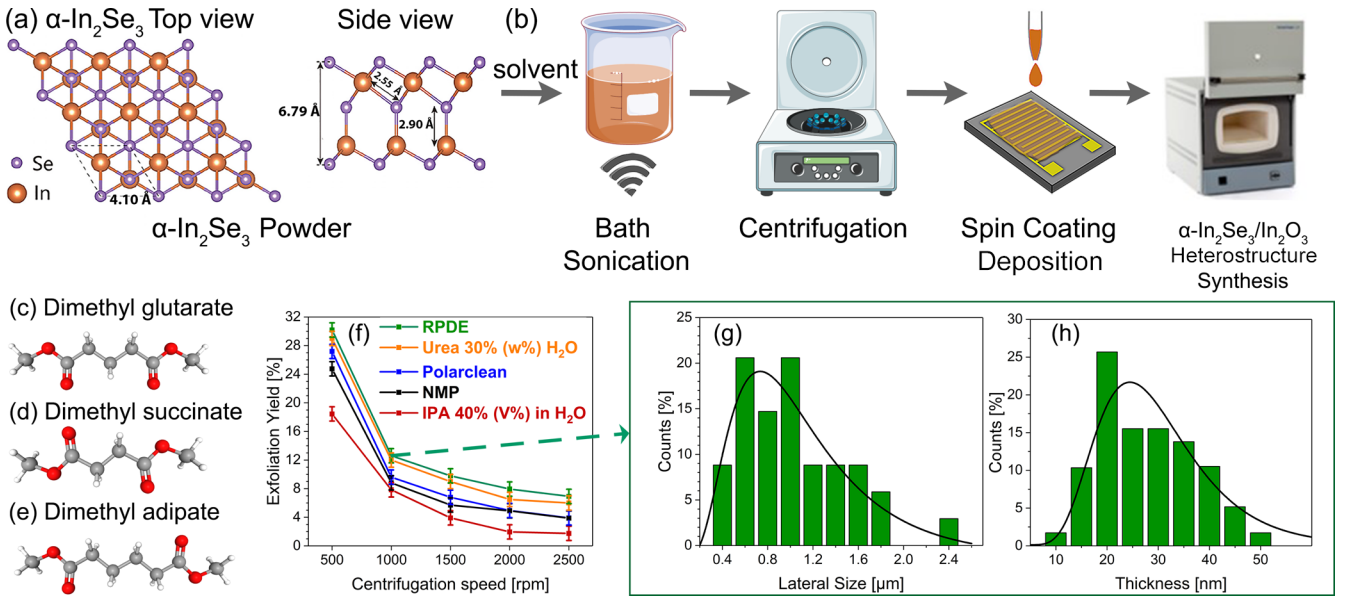

Figure 1. (a) Planar and side views of the Se−In−Se−In−Se quintuple layer blocks of the crystal structure of the *a*-In_2Se_3 phase. Reproduced from ref 21: Nian, T.; Wang, Z.; Dong, B. Thermoelectric Properties of *α*-In_2Se_3 monolayer. *Appl. Phys. Lett.* **2021,** *118*(3). Copyright 2021 AIP Publishing; (b) schematization of the sonication-assisted LPE process comprising spin-coating deposition of the flakes over interdigitated patterns and thermal treatment in air at 180 °C for 24 h to synthesize the *a*-In_2O_3/In_2Se_3 heterostructure; (c−e) ball-and-stick representation of the Rhodiasolv RPDE solvent's main constituents (red: oxygen, gray: carbon, and white: hydrogen); (f) exfoliation yield (%) as a function of the centrifugation speed after 15 min for different solvents (RPDE, PolarClean, NMP, urea 30% (w %) in water, and 40% IPA in water). (g,h) SEM and AFM statistical analysis of the lateral size and thickness distribution of RPDE exfoliated In_2Se_3 flakes corresponding to 1000 rpm and 15 min centrifugation.

substitution of the chalcogen atoms (S, Se, and Te) operated by ambient O_2 ($\Delta G < 0$), is an inexplicably overlooked issue when exploiting new TMDs and MCs platform interfaces for electronic applications. Specifically, the surface degradation process, eventually accelerated at high OTs, is responsible, in the long run, for irreversible drift phenomena of the electrical response (i.e., sensor signal creep), limiting the exploitation of these interfaces.

In the case of binary III−IV group 2D-layered semiconductor selenides, the spontaneous oxidation process initiates with the formation of an amorphous skin of *a*-MO_x (M = In, Ga, Sn, Ge) advancing from the surface toward the inner layers as reported for InSe,[10] GaSe,[11] GeSe,[12] and SnSe,[13] addressing new strategies to passivate the sensor surface from fast degradation.

We have recently reported[14,15] a successful synthesis, which passivates the nanoplate's surface, yielding the formation of either a protective amorphous metal-oxide skin layer of *a*-SnO_2 over 2D-$SnSe_2$ to produce *a*-$SnO_2/SnSe_2$ heterojunctions or fully *a*-SnO_2 2D layered amorphous interfaces, with excellent long-term stability of the baseline resistance and excellent sensor' signal (i.e., R_a/R_g) reproducibility.

In this work, we demonstrate that the passivation/amorphization thermal oxidation process can be successfully extended to liquid-phase exfoliated commercial powders of binary III−IV group vdW 2D-In_2Se_3 semiconductor chalcogenides yielding *a*-In_2O_3/In_2Se_3 heterostructures, with unveiled H_2 and NO_2 responses in air/humid atmospheres.

We specifically report a liquid-phase exfoliation (LPE) procedure utilizing for the first time the Rhodiasolv RPDE eco-friendly commercial solvent to synthesize few layers of 2D-In_2Se_3 (20−30 nm thick) subsequently annealed in air at 180 °C for 24 h to promote the formation of the *a*-In_2O_3/In_2Se_3 heterostructure. This paper, besides the effectiveness of the passivation synthesis here validated, highlights that self-assembled 2D-amorphous/2D-crystalline heterostructures can detect oxidizing (NO_2) and reducing (H_2) gases in the same way as chemoresistive MO sensors, opening new perspectives to exploit the gas sensing properties of amorphous MO interfaces.

2. EXPERIMENTAL SECTION

2.1. 2D In_2Se_3 Exfoliation. In_2Se_3 crystals (Ossila—UK) were exfoliated in *N*-methyl-2-pyrrolidone (NMP, Sigma-Aldrich), Rhodiasolv RPDE (Solvay Novecare), Rhodiasolv PolarClean (Solvay Novecare), IPA (Sigma-Aldrich) 40 vol % in H_2O and Urea (Sigma-Aldrich) 30 wt % in H_2O, following a sonication-assisted LPE method comprising three steps:

(i) *In_2Se_3exfoliation.* After 5 min of mortar grinding, 10 mg of In_2Se_3 were dispersed in 20 mL of the chosen solvent inside a 50 mL Falcon tube and isothermally bath sonicated at 24 ± 2 °C for 3 h (Elmasonic P60H at a 37 kHz frequency).

(ii) *Solvent removal and purification.* After the first centrifugation (Neya 8 Bench Top centrifuge) at 5500 rpm for 15 min, two-thirds of the initial solvent were removed and replaced with ethanol (Sigma-Aldrich). After redispersion by sonication, three more rounds were carried out at 5000 rpm with subsequent replacement of the supernatant with fresh ethanol to ensure complete removal of the exfoliating medium.

(iii) *Exfoliation yield.* To separate the exfoliated material, 15 min centrifugations were performed at different speeds (500, 1000, 1500, 2000, and 2500 rpm). Then, the 9/10 of the supernatant of each dispersion was taken by pipetting and dried overnight on a laboratory watch glass at 90 °C. Exfoliation yield [%] was calculated as the ratio between the initial and the final mass of the exfoliated dried material.

2.2. Synthesis of the 2D *a*-In_2O_3/In_2Se_3 Heterostructure. The 2D *a*-In_2O_3/In_2Se_3 heterostructure was synthesized by annealing the as-exfoliated nanosheets in static air at 180 °C for 24 h. After thermal

https://doi.org/10.1021/acsanm.3c00380
ACS Appl. Nano Mater. 2023, 6, 6011−6023

Table 1. Surface Tensions (m[N/m]) and Exfoliation Yields (%), Calculated as the Percentage Ratio of the Weight of the Flakes in the Final Dispersion with Respect to the Initial One, upon 1000 rpm and 15 min Centrifugation with Different Solvents, Utilizing WS_2 and In_2Se_3 Commercial Powders

Solvent	Rhodiasolv RPDE	Rhodiasolv PolarClean	*N*-methyl-2-pyrrolidone (NMP)	IPA 40% (V %)H_2O	Urea 30% w H_2O
surface tension σ_S m[N/m]	67[17]	38[22]	40[18]	36[20]	74[23]
In_2Se_3 exfoliation yield [%]	13.0 ± 0.6	9.9 ± 0.7	8.6 ± 0.6	8.0 ± 0.7	12.8 ± 0.8
WS_2 exfoliation yield [%]	5.0 ± 0.6	16.2 ± 0.7	14.7 ± 0.6	13.4 ± 0.7	4.7 ± 0.8

treatment, flakes were redispersed in ethanol and deposited by spin coating over dedicated substrates for further characterization.

2.3. Microstructural Characterization. Exfoliated In_2Se_3 microstructural features were investigated using SEM (Gemini FE-SEM 500), high-resolution transmission electron microscopy (HRTEM), and SAED at 200 kV by JEOL JEM 2010F (JEOL Ltd., Tokyo, Japan) and tapping-mode atomic force microscopy (AFM) (NT-MDT Ntegra, Spectrum). Thermogravimetric (TG—DTA) analyses were performed in air and N_2 atmospheres using LINSEIS L81-I (Linseis GmbH, Germany). XPS spectra were collected using a PHI 1257 spectrometer with a monochromatic Al Kα source ($h\nu$ = 1486.6 eV) at a 250 meV spectral resolution. Grazing-incidence X-ray diffraction was performed using XRD-PAN Analytical X'PERT Pro with Cu Kα_1 radiation (λ = 1.5406 Å) with an incident angle of 0.8°. A PerkinElmer Lambda 1050 + UV/vis/NIR spectrophotometer (PerkinElmer Inc., Waltham, USA) equipped with a 100 mm integrating sphere was utilized for optical characterization. Reflectance spectra were collected in diffuse reflectance spectroscopy (DRS) configuration, and the Kubelka−Munk function was utilized to elaborate the signal.

2.4. Electrical Characterization. 30 μL of the 2D a-In_2O_3/In_2Se_3 nanosheets dispersion were spin-coated over Si_3N_4 substrates provided with Pt finger-type electrodes (30 μm apart) and backside heater placed inside a Teflon test cell (500 cm^3). Electrical resistance was measured (Agilent 34970A) at different OTs (25−150 °C range), as shown in Figure S1. Distinct gas concentrations were obtained by diluting certified mixtures (Nippon gases—IT) of NO_2 (5 ppm in pure air) and H_2 (250 ppm in pure air) with synthetic dry air utilizing mass flow controllers (MKS147), setting the total flow rate at 500 sccm/min. Different relative humidities (RH %) were obtained by mixing dry air with water-saturated air at 25 °C (i.e., RH % @ 25 °C). The RH % (RH % @ 25 °C) was measured before injecting the humid air into the test cell by using a thermo-hygrometer (HI9564, Hannah Instruments, Padua—IT). Exfoliated In_2Se_3 gas sensing properties were assessed by using the following figures of merit: (i) baseline resistance (BLR): the sensor's resistance in air at equilibrium; (ii) sensor's signal: the relative resistances changes (R_{Gas}/R_{Air}) and (R_{Air}/R_{Gas}) to oxidizing/reducing gases; (iii) sensor sensitivity (S): the slope of the calibration curve in the log−log plot, (iv) adsorption and desorption times (τ_{ADS}, τ_{DES}): the time needed to reach 90% of the sensors' signal steady-state value after gas adsorption or desorption.

3. RESULTS AND DISCUSSION

3.1. In_2Se_3 Material Exfoliation. We exfoliated (Figure 1a) commercial crystals of α-In_2Se_3 by sonication-assisted LPE, collecting flakes with different lateral sizes and thicknesses depending on the centrifugation speed and time. The centrifuged suspension, after purification with ethanol, was spin-coated over interdigital electrodes and annealed in air at 180 °C for 24 h to promote the formation of the a-In_2O_3/In_2Se_3 heterostructures. LPE exfoliation was carried out for the first time, utilizing Rhodiasolv RPDE, an eco-friendly and nontoxic commercial dibasic ester solvent,[16] with a chemical composition comprising three different dimethyl ester molecules (Figure 1c−e), as confirmed by Fourier transform infrared (FTIR) spectroscopy analysis shown in Figure S2 and product's data sheet specifications.[17] The RPDE solvent's exfoliation yield (calculated for each centrifugation speed/time, as the percentage ratio of the weight of the flakes in the final dispersion with respect to the initial one), is shown in Figure 1f, with those obtained utilizing toxic NMP,[18] sustainable water soluble Rhodiasolv PolarClean,[19] 40 vol % IPA in water,[20] and Urea 30 wt % in water. The RPDE solvent exhibits better exfoliation yields (green line in Figure 1f) with respect to the others, demonstrating to be an excellent substitute for NMP and a suitable alternative to PolarClean. Finally, the centrifugation speed and time tune the morphology of the exfoliated In_2Se_3. Flakes' lateral size and thickness distributions, corresponding to a 1000 rpm centrifuge speed, are shown in Figures 1g,h and S3, with a calculated "aspect ratio" (AR) of ∼40 (AR = flakes lateral dimension/flakes thickness).

The exfoliation yields of different representative solvents, using In_2Se_3 and WS_2 as reference materials, upon 1000 rpm and 15 min centrifugation are compared in Table 1. RPDE and 30% (w %) urea/water are more effective in exfoliating In_2Se_3 (∼13%) with respect to WS_2 (∼5%). Conversely, PolarClean, NMP, and 40% (V %) IPA/water are more suitable to exfoliate WS_2 (∼14% average) than In_2Se_3 (∼9% average).

It is reported that, to exfoliate vdW solids, the enthalpy of mixing between the nanosheet's solid surface and the solvent must be minimized, predicting that the surface energy of the nanosheet (E_{NS}) be comparable to the total (polar and dispersive) surface energy of the solvent (E_S).[24] Considering now the total solvent's surface energy as

$$E_S = (\sigma_S + TS_{Surf})$$

where σ_S is the solvent's surface tension and S_{surf} is the surface entropy (∼0.1 m[N/(m K)] for liquids); setting TS_{Surf} ∼ 30 m[J/m^2] for almost all liquids at 20 °C,[25] it turns out that solvent's surface energies E_S are ∼30 m[J/m^2] higher than their surface tension σ_S. Consequently, the surface tension σ_S shown in Table 1 must be increased by a factor of 30 m[J/m^2] before matching E_S with E_{NS}. On this account, PolarClean, NMP, and IPA, with E_S ∼ 70 m[J/m^2], which is approximately the same order as that of WS_2 nanosheets E_{NS} ∼ 75 m[J/m^2],[26] possibly explain their superior capability to exfoliate WS_2, with respect to the others. Conversely, RPDE and urea with associated surface energies of 97 and 104 m[J/m^2] are more effective in exfoliating In_2Se_3 than WS_2. A tentative explanation, although not entirely satisfactory, could be that In_2Se_3 nanosheets' surface energy E_{NS} is slightly higher than those reported for TMDs (70−80 m[J/m^2]), therefore much closer to the surface energy of RPDE and urea solvents than to the others. Data on the surface energy of In_2Se_3 are quite scarce. Proxies to estimate the unknown In_2Se_3 surface energy value could be tentatively those theoretically computed for GaSe and GeSe group III−IV mono-selenides, yielding ∼145 and ∼220 m[J/m^2], respectively.[27] These values are slightly higher than those predicted for 2D TMDs materials, possibly supporting the

https://doi.org/10.1021/acsanm.3c00380
ACS Appl. Nano Mater. 2023, 6, 6011−6023

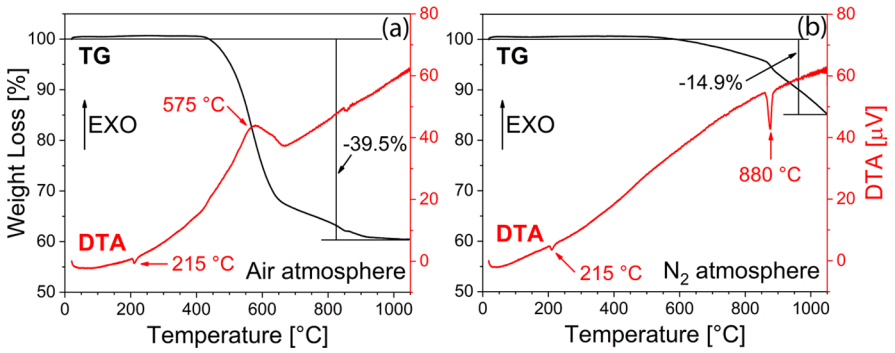

Figure 2. TG (black line) and DTA (red line) signals of as-exfoliated In_2Se_3 flakes performed in air (a) and nitrogen (b) atmospheres in the 25−1050 °C temperature range, with a heating rate of 5 °C/min.

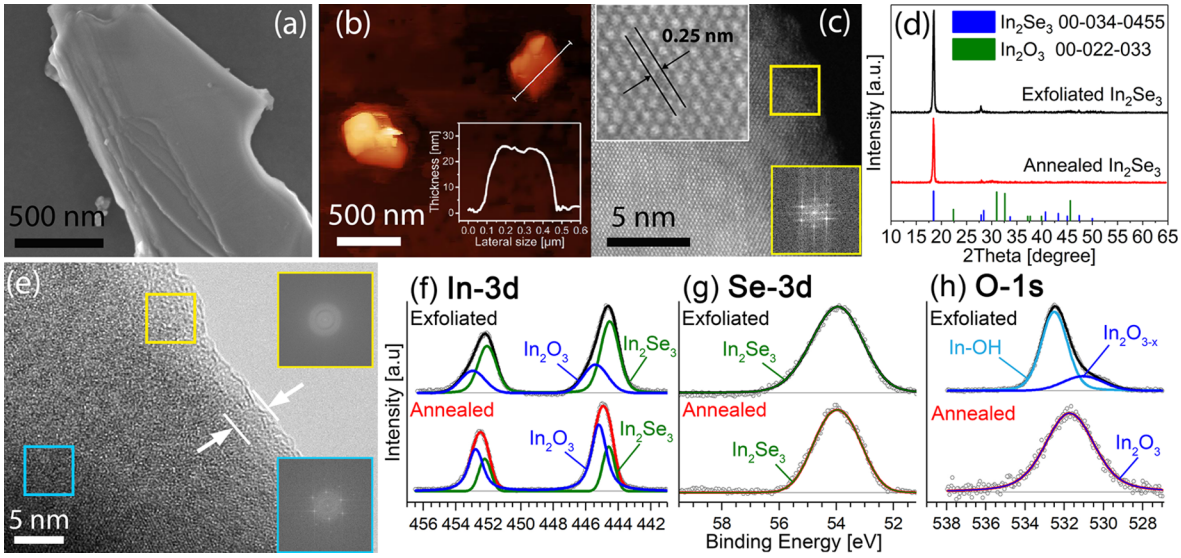

Figure 3. (a) SEM image of few flakes of exfoliated In_2Se_3; (b) AFM picture of exfoliated In_2Se_3 flakes with an associated thickness profile; (c) HRTEM image of exfoliated In_2Se_3 flakes. Top left inset exhibiting an interplane distance of 0.25 nm corresponding to the (006) interplane distance of In_2Se_3; (d) grazing-incidence XRD pattern of exfoliated and annealed (at 180 °C for 24 h) samples; (e) HRTEM image of annealed In_2Se_3 flakes exhibiting an *a*-In_2O_3 amorphous layer at the edge (white arrows). SAED patterns collected at the edge (yellow) and corresponding to the center of the flake (blue); (f−h) XPS spectra of as-exfoliated (top) and annealed (bottom) flakes: (f) In 3d, (g) Se 3d, and (h) O 1s core-level spectra.

better performances of RPDE and urea solvents to exfoliate In_2Se_3.

3.2. Synthesis of the *a*-In_2O_3/In_2Se_3 Heterojunction. The thermal oxidation properties of In_2Se_3 exfoliated flakes, annealed at 5 °C/min in static air and N_2 from 25 to 1050 °C, have been recorded by TG-DTA simultaneous analysis and shown in Figure 2a,b. No significant weight changes are recorded up to 450 °C temperature in air and in N_2, respectively. DTA signals exhibit a modest endothermic peak at 215 °C, ascribed to the transition from *α*-In_2Se_3 to *β*-In_2Se_3.[21,28]

Overall, the TG analysis in air shows a total weight loss of −39.5 ± 0.6%, starting at 450 °C, topping a maximum rate at 575 °C, as indicated by the exothermic DTA peak in Figure 2a. Remarkably, the recorded weight loss of −39.5 ± 0.6% is significantly close to the theoretical weight loss of −40.49% corresponding to the formation of In_2O_3. In the same way as to thermal oxidation in air of 2D $SnSe_2$ and 2D WS_2 yielding SnO_2 and WO_3,[15,29] the formation of In_2O_3 proceeds by the complete substitution of the chalcogen atoms (Se) operated by ambient O_2 according to a thermodynamic spontaneous process ($\Delta G < 0$). In N_2 atmosphere, the weight loss of −14.9 ± 0.6% possibly accounts for the sublimation of Se atoms in a similar way to the mechanism discussed for $SnSe_2$.[15] Finally, the sharp DTA endothermic peak at 880 °C is attributed to the melting of In_2Se_3.[30] Exfoliated *α*-In_2Se_3 flakes have been subjected to a controlled oxidation process at 180 °C in air for 24 h at temperatures below the recrystallization temperature of the native oxide (270−300 °C) to promote the formation an amorphous self-assembled *a*-In_2O_3 skin layer over the 2D-In_2Se_3 flakes.

Figure 3 shows the microstructural features of the flakes before (Figure 3a−c) and after (Figure 3e) annealing, including the corresponding XRD (Figure 3d) and XPS (Figure 3f−h) spectra. Overall, exfoliated In_2Se_3 exhibits a stacked-layer morphology (Figure 3a,b) with lateral sizes larger than 500 nm and thicknesses between 25 and 30 nm (see also Figure 1g,h for flakes' size statistics), corresponding to ∼30 layers (assuming flake's thickness of 6.79 Å and interspace distances of 2.87 Å[21]).

HRTEM analysis of the as-exfoliated In_2Se_3 shown in Figure 3c exhibits a highly ordered crystalline texture extending to the

https://doi.org/10.1021/acsanm.3c00380
ACS Appl. Nano Mater. 2023, 6, 6011−6023

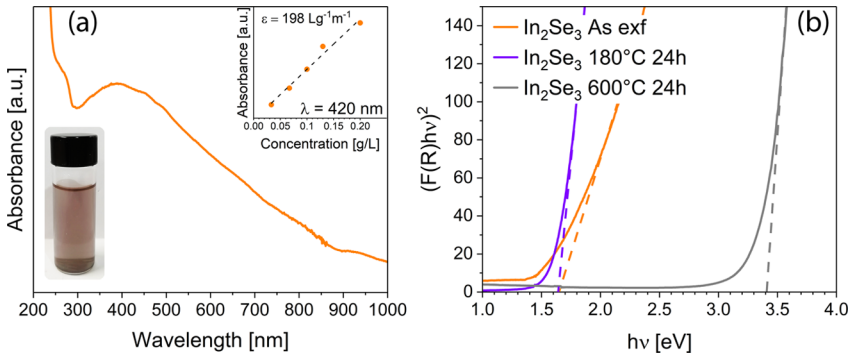

Figure 4. Optical characterization of as-exfoliated and annealed In_2Se_3; (a) UV−vis absorption spectrum of as-exfoliated In_2Se_3. Inset: absorbance coefficient estimated at 420 nm; (b) Tauc plot and BG determination of as-exfoliated and annealed In_2Se_3.

edge of the flake, as confirmed by SAED patterns (yellow square area of the figure). An interplane distance of 0.25 nm (top left inset) corresponding to In atoms tetrahedrally coordinated in a rhombohedral ($R3m$) symmetry of the α-In_2Se_3 phase[28] is clearly visible. Such a crystalline structure is confirmed by XRD characterization shown in Figure 3d (black plot), exhibiting, at $2\Theta = 18.4°$, the characteristic (006) plane orientation of α-In_2Se_3 (JCPDS card 00-034-0455).

After annealing at 180 °C for 24 h (Figure 3e), SAED patterns (yellow square) exhibit the formation of an amorphous boundary layer structure approximately 5−7 nm thick, extending from the edge to the center of the flake. The formation of an amorphous a-In_2O_3 skin, growing over the underlying 2D In_2Se_3 flake, is attested (see the electronic magnification of Figure 3e) by the existence of a disordered structure self-assembled over the whole flake. Remarkably, SAED patterns (blue square) corresponding to the center of the flake confirm the crystalline reflections of the underlying In_2Se_3, attesting the formation of the a-In_2O_3/In_2Se_3 amorphous/crystalline heterostructure. Additionally, XRD patterns of the annealed flakes (red plot of Figure 3d) highlight a slight reduction of the (006) peak's area of In_2se_3 because of the proceeding of the amorphization process and the absence of new crystalline phases.

Figure 3f−h compares the XPS features of the as-exfoliated and annealed films. The deconvolution of the In 3d core-level spectrum of the exfoliated sample exhibits two contributions having their 5/2 components peaked at the binding energies (BEs) of 444.7 eV (green line) and 445.6 eV (blue line), which can be ascribed to In_2Se_3[31] and In_2O_3[32] phases, respectively, with the former covering 75% of the total spectral area and the latter associated with the remaining 25%. After annealing at 180 °C for 24 h, the opposite takes place. The In_2O_3 oxide signal covers 73% of the spectral area, while In_2Se_3 has a residual of 27%. Unsurprisingly, considering that XPS information comes from photoelectrons escaping a maximum of up to 10 nm, the occurrence in the In 3d spectra of both signals of In_2O_3 and In_2Se_3 is further evidence that the a-In_2O_3 oxide thickness is limited within 5−7 nm as previously determined by HRTEM characterization (Figure 3e). Regarding the Se 3d spectra, only a single contribution is found in both samples, with its 5/2 component centered at a BE of 54.1 eV corresponding to Se−In bonds in the In_2Se_3 structure.[31] Remarkably, the absence of any features at higher binding energies, specifically at ∼58.6 eV attributed in a previous paper[31] to Se−O bonds, rules out the formation of Se-oxidized phases, indicating that all the Se-bonds belong to In_2Se_3. Moreover, the formation of an oxide layer over the annealed sample with respect to the exfoliated sample accounts for an attenuation of the Se 3d signal's area of ∼30%. Finally, the O 1s core-level spectra of the as-exfoliated sample (Figure 3h) can be deconvoluted in two different contributions. The lower BE of 531.2 eV, related to defective In_2O_3, namely, In_2O_{3-x} (where $0 \leq x \leq 1$), corresponds to oxygen defects in the matrix of indium oxide,[33] the higher BE, peaking at 532.5 eV, is compatible with hydroxide-related species, as recently described for In-based films.[34] However, after annealing, a clear single contribution centered at 531.9 eV, associated with In_2O_3, excludes the formation of any mixed $In_2Se_{3-3x}O_{3x}$ ($0 \leq x \leq 3$) oxide phase as previously reported.[31] It may be concluded that both microstructural characterization and chemical composition confirm that annealing at 180 °C for 24 h successfully induces the formation of 5−7 nm thick, amorphous a-In_2O_3 skin-layer oxide. The a-In_2O_3/In_2Se_3 amorphous/crystalline heterostructure passivates the underlying 2D-In_2Se_3 from further degradation, as will be demonstrated by electrical characterization.

3.3. Electrical Properties and Gas Sensing Response.

2D few-layered In_2Se_3 has attracted much attention due to its excellent properties and tunable band gaps (BGs) depending on the number of the layers, ranging from ∼1.5 to 1.7 eV for few layers[35] to 2.27 eV for thin-film photoanodes.[36] Optical BG measurements of as-exfoliated and samples annealed at 180 and 600 °C have been carried out by DRS applying the Kubelka−Munk theory. UV−vis characterization has been performed on ethanol dispersion of as-exfoliated In_2Se_3 flakes (0.2 g/L) as shown in Figure 4a.

The as-exfoliated sample broadly absorbs in the whole UV−vis region, with an absorption band edge placed around 850 nm, consistent with In_2Se_3 mixed nanoparticles−nanorods.[37] Moreover, both the ∼400 nm peak and the calculated absorption coefficient [i.e., of 198 L/(g·m)] well agree with those reported for NMP-LPE In_2Se_3 nanosheets.[38] Transforming the diffuse reflectance spectra into relative absorption plots using the Kubelka−Munk function,[39] samples' BGs are graphically computed from Figure 4b utilizing Tauc's equation[40]

$$(F(R)h\nu)^{1/\gamma} = B(h\nu - E_g)$$

where h is Planck's constant, ν is the incident photon energy, E_g is the optical BG energy, and B is a constant. Assuming a γ factor of 1/2 corresponding to a direct BG transition for In_2Se_3 nanosheets, the extrapolation of Tauc's plots, calculated over five different samples, yields 1.65 ± 0.02, 1.64 ± 0.03, and 3.41

https://doi.org/10.1021/acsanm.3c00380
ACS Appl. Nano Mater. 2023, 6, 6011−6023

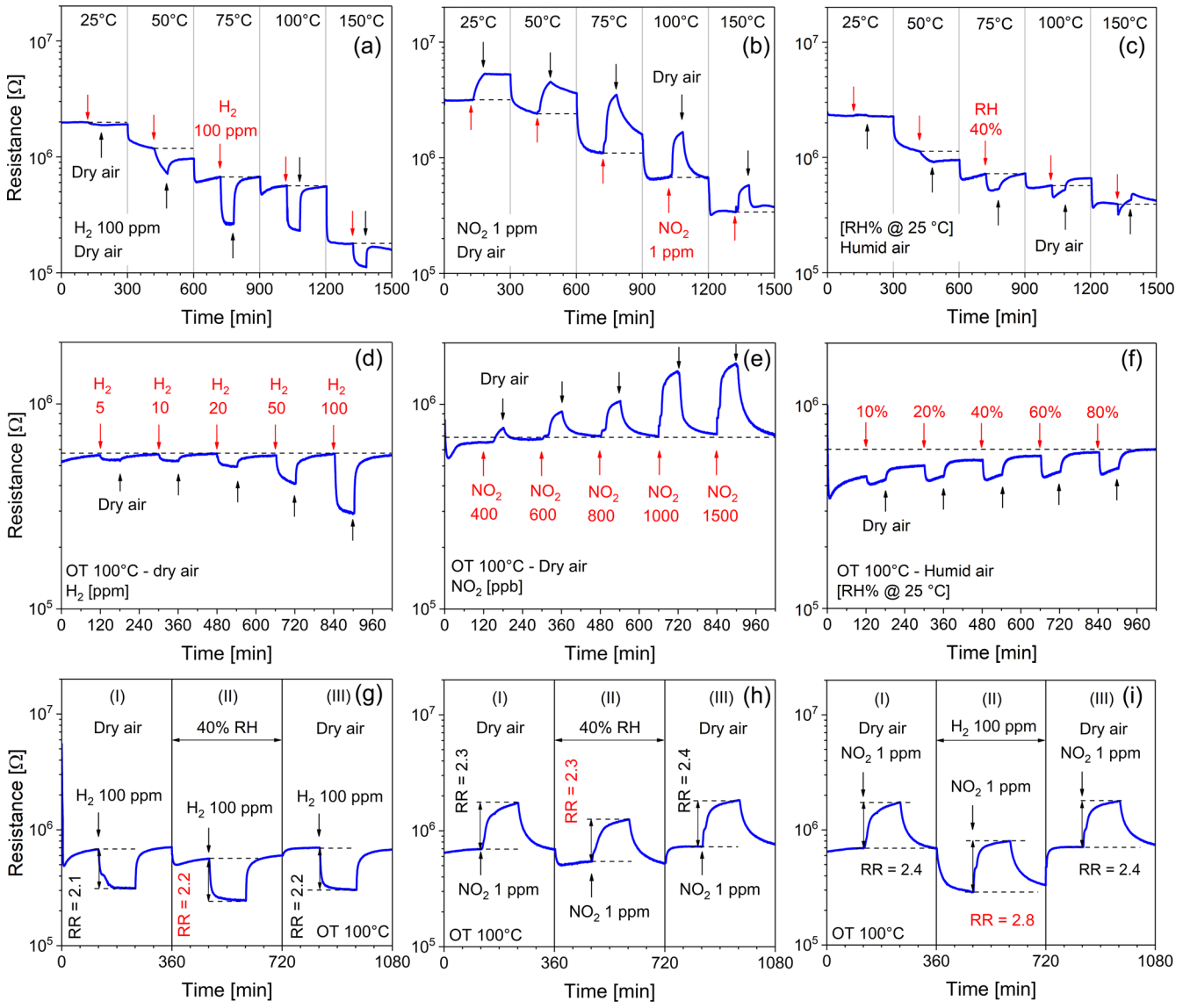

Figure 5. Electrical responses in dry air of a-In_2O_3/In_2Se_3 thin films at different OTs (from 25 to 150 °C) to (a) 100 ppm H_2, (b) 1 ppm NO_2, and (c) 40% humidity (RH @ 25 °C); (d–f) dynamic electrical responses in dry air at 100 °C OT to (d) H_2 (5–100 ppm), (e) NO_2 (400 ppb–1.5 ppm), and (f) H_2O in the range of 10–80% RH (RH at 25 °C). (g) 40% RH humidity cross to 100 ppm H_2: (I) first step in dry air and 100 ppm H_2; (II) second step at 40% RH background and 100 ppm H_2; (III) third step, equivalent to (I), to assess short-term repeatability. (h) 40% RH humidity cross to 1 ppm NO_2: (I) first step in dry air and 1 ppm NO_2; (II) second step at 40% RH background and 1 ppm NO_2; (III) third step, equivalent to (I), (i) 100 ppm H_2 cross to 1 ppm NO_2 (I) first step in dry air and 1 ppm NO_2, (II) second step at 100 ppm H_2 background and 1 ppm NO_2, (III) third step, equivalent to (I).

± 0.03 eV of the as-exfoliated and 180- and 600 °C-annealed In_2Se_3, respectively. The ∼1.65 eV BG of the as-exfoliated In_2Se_3 well fits with reported values of exfoliated 2D In_2Se_3 flakes, with thicknesses ranging from 3 to 28 nm.[35] Most strikingly, the calculated BG of the a-In_2O_3/In_2Se_3 heterojunction, corresponding to the 180 °C-annealed sample, is ∼1.64 eV, which is approximately the same of the exfoliated In_2Se_3. Data about BG values of amorphous a-In_2O_3 are quite scarce, making the discussion not this straightforward. However, the occurrence of defects in the amorphous structure of a-In_2O_3 could entail the formation of intermediate states within the a-In_2Se_3 electronic structure, eventually tuning the BG of a-In_2O_3 much closer to that of In_2Se_3 than crystalline In_2O_3.[31] Another possible explanation could be that the as-grown a-In_2O_3 skin with an associated thickness of 5–7 nm is too thin to significantly alter the optical properties of the sample. Finally, the ∼3.41 eV BG of the 600 °C-annealed flakes is congruent with the value of ∼3.45 eV, reported for sintered crystalline In_2O_3 thin films prepared by spray pyrolysis.[41]

Electrical tests of the a-In_2O_3/In_2Se_3 flakes have been carried out in dry/wet air background [0–80% relative humidity (RH at 25 °C)], H_2 (5–100 ppm), and NO_2 (0.4–1.5 ppm) at 100 °C OT. Figure 5a–c displays the electrical responses of a-In_2O_3/In_2Se_3 thin films in dry air to 100 ppm H_2, 1 ppm NO_2, and 40% RH, respectively, in the OT range of 25–150 °C. The best OT at 100 °C has been selected as a trade-off between the need to regain the BLR (the resistance in air at equilibrium after gas desorption—dotted black lines of Figure 5a–c) and the requisite to yield satisfactory sensor signal variations (i.e., R_a/R_g and R_g/R_a). Increasing the temperature improves the recovery of the BLR, while reducing the temperature causes

https://doi.org/10.1021/acsanm.3c00380
ACS Appl. Nano Mater. 2023, 6, 6011–6023

irreversible adsorption of gas molecules, as frequently experienced in MO and 2D layered sensors.[42] Best OTs are found at 75 and 100 °C for H_2 and NO_2, respectively. The lower hydrogen's OT appears to be related to the smaller electron affinity of H_2 (0.18 eV) with respect to NO_2 (2.3 eV), which facilitates faster desorption. Moreover, sensor's electrical resistances decrease/increase upon exposing it to H_2/NO_2 gases, confirming an *n*-type response mechanism of the *a*-In_2O_3/In_2Se_3 heterojunction. Accordingly, water vapor behaves as a reducing gas, with the best OT at 75 °C (Figure 5c). Overall, the passivation thermal treatment of In_2Se_3 flakes at 180 °C stabilizes the *a*-In_2O_3/In_2Se_3 heterojunction when operating at lower temperatures (75−100 °C), providing, at the same time, an effective solution for fast adsorption/desorption, excellent BLR recovery, and improved sensor's signal reproducibility.

Dynamic gas responses in the dry-air background to H_2, NO_2, and different RHs shown in Figure 5d−f exhibit a decrease/increase of the electrical resistance with increasing H_2/NO_2 concentrations and excellent baseline recovery. In dry air carriers, the experimental limit of detection (LOD) to H_2 is 5 ppm, one of the smallest ever reported for 2D exfoliated TMD and MC interfaces (see Table 2 for comparisons). That to NO_2 is even smaller (400 ppb) considering the stronger attitude of NO_2 to withdraw electrons from the surface. The sensor signal, defined as the ratio R_a/R_g or R_g/R_a depending on the reducing/oxidizing nature of the gas, is 2.1 ± 0.2 to 100 ppm H_2 and 2.3 ± 0.2 to 1 ppm NO_2, providing a ±0.2 uncertainty calculated over a set of five identical measurements. These results are comparable to H_2 and NO_2 responses of *a*-$SnO_2/SnSe_2$ heterostructures and fully amorphous *a*-SnO_2 2D interfaces, as previously reported.[14,15]

Table 2. Comparison of the H_2 Gas Sensing Performances of Different Sensor's Interfaces Obtained by Normalizing Literature Data to 10 ppm H_2 in Dry Air

Sensing material and structure	LOD [ppm][a]	RRs 10 ppm H_2[b]	OT [°C]	refs
MOS−Noble Metal/MOS−MOS Heterostructures				
In_2O_3 mesoporous	0.1	1.8	260	43
Au−In_2O_3 core−shell	2	5.0	300	44
Au−SnO_2 nanoparticles	5	6.2	250	45
Pd−SnO_2 nanofibers	0.25	12.6	160	46
CeO2−In_2O_3 hollow sphere	1	12.2	160	47
NiO−ZnO nanofibers	5	1.5	200	48
2D-Graphene (G-GO-rGO)−NP-Decorated/G-rGO				
G-decorated Pd NCL	0.1	1.06	25	49
rGO-decorated Pt NPs	1	1.04	25	50
G-decorated SnO_2 NPs	1	2.00	50	51
2D TMDs−MCs.−NP-Decorated/TMDs−MCs				
Pt NPs−MoS_2	10	1.20	150	52
2D−MoS_2	10	1.10	25	53
Pd−SnO_2/MoS_2	30	1.02 (@100 ppm)	25	54
Pd NPs−MoS_2	50	1.18 (@100 ppm)	25	55
2D TMDs−MCs−Heterostructures				
a-WO_3/WS_2 amorphous/cryst	5	2.80	150	29
a-$SnO_2/SnSe_2$ amorphous/cryst	5	1.22	100	14
a-In_2O_3/In_2Se_3 amorphous/cryst	5	1.20	100	this work

[a]Experimental LOD. [b]RR = R_a/R_g for *n*-type and R_g/R_a for *p*-type sensors.

Cross-sensitivity tests, aimed to assess the variation of the sensor's signal to H_2 or NO_2 target gases when humidity is the interfering one, are shown in Figure 5g,h. According to a standardized procedure, in the first step (I), the sensor is exposed to a dry-air background and the target gases (100 ppm H_2 or 1 ppm NO_2); in the second step (II), it is exposed to a 40% RH background and target gases; in the third step (III), the sensor is exposed to the same sequence as to (I) to assess the short-term repeatability. According to Figure 5g,h, the BLR always decreases when the sensor is exposed to humidity. Remarkably, sensor's signals (i.e., RRs) to both H_2 and NO_2 gases are almost the same in dry air and 40% RH backgrounds. Specifically, sensor's signal yields RR = 2.1 ± 0.2 and RR = 2.3 ± 0.2 to 100 ppm H_2 and 1 ppm NO_2, respectively, regardless of the humidity content (RH at 40%), apparently suggesting no cross-interference of water vapor to H_2 and NO_2 sensing. In the second run, shown in Figure 5i, the H_2 cross-interference to the NO_2 target gas is displayed. Specifically, the sensor signal to 1 ppm NO_2 significantly increases from RR = 2.4 ± 0.2 in dry air to RR = 2.8 ± 0.2 in the 100 ppm H_2 background. Finally, *a*-In_2O_3/In_2Se_3 exhibits excellent short-term repeatability properties, as attested by comparing the electrical responses of panel (I) and panel (III) for all the investigated sequences. The selectivity response, obtained by comparing the sensor's RRs to 100 ppm H_2 and 1 ppm NO_2 in dry air, with respect to different gases and organic vapors, is also shown in Figure S6. The humidity cross-interference to 100 ppm H_2 and 1 ppm NO_2 target gases in the whole 0−80% RH range is displayed in Figure 6a,b. Remarkably, sensor's signal response to 100 ppm H_2 is the same in the humidity range of 0−60% while that to NO_2 remains constant in a narrower range (0−40%). These results confirm, as previously found by cross-test investigations (Figure 5g,h), that no cross-sensitivity effects of water vapor are detectable in the 0−40% range for both gases.

Notably, with increasing RH (as to the direction of the red arrow of Figure 6a,b), water vapor inhibits/enhances the H_2/NO_2 sensor's signal, displaying an antisynergistic/synergistic effect upon sensor's signal amplitude. Specifically, signal responses to 100 ppm H_2 decrease from 2.1 ± 0.2 to 1.7 ± 0.2 from 0 to 80% RH. Conversely, that to 1 ppm NO_2 increases from 2.4 ± 0.2 to 3.8 ± 0.2. The log−log calibration plots of the sensor's signal (i.e., R_a/R_g for H_2 and R_g/R_a for NO_2) in the whole gas concentration range and different RH values are shown in Figure 6d,e. At RH % higher than 60 and 40%, the calibrating H_2 and NO_2 lines shift downward/upward (as to the direction of the red arrows of Figure 6d,e), respectively. Congruent with this tendency, water vapor has a remarkable effect to change the LOD. Specifically, the decrease/increase of the H_2/NO_2 slopes of the calibrating lines at 80% RH (with respect to that at 0% RH) downshifts/upshifts the theoretical LOD (obtained by graphically extrapolating the calibrating lines to the intercept drawn at RR = 1). Most strikingly, a high level of humidity has a strong influence on the adsorption time. Increasing the RH increases/decreases the adsorption times to H_2 and NO_2 as shown in Figure 6c.

Combining these observations, it may be concluded that depending on the reducing/oxidizing nature of the interfering gas, provided an *n*-type response of the *a*-In_2O_3/In_2Se_3

https://doi.org/10.1021/acsanm.3c00380
ACS Appl. Nano Mater. 2023, 6, 6011−6023

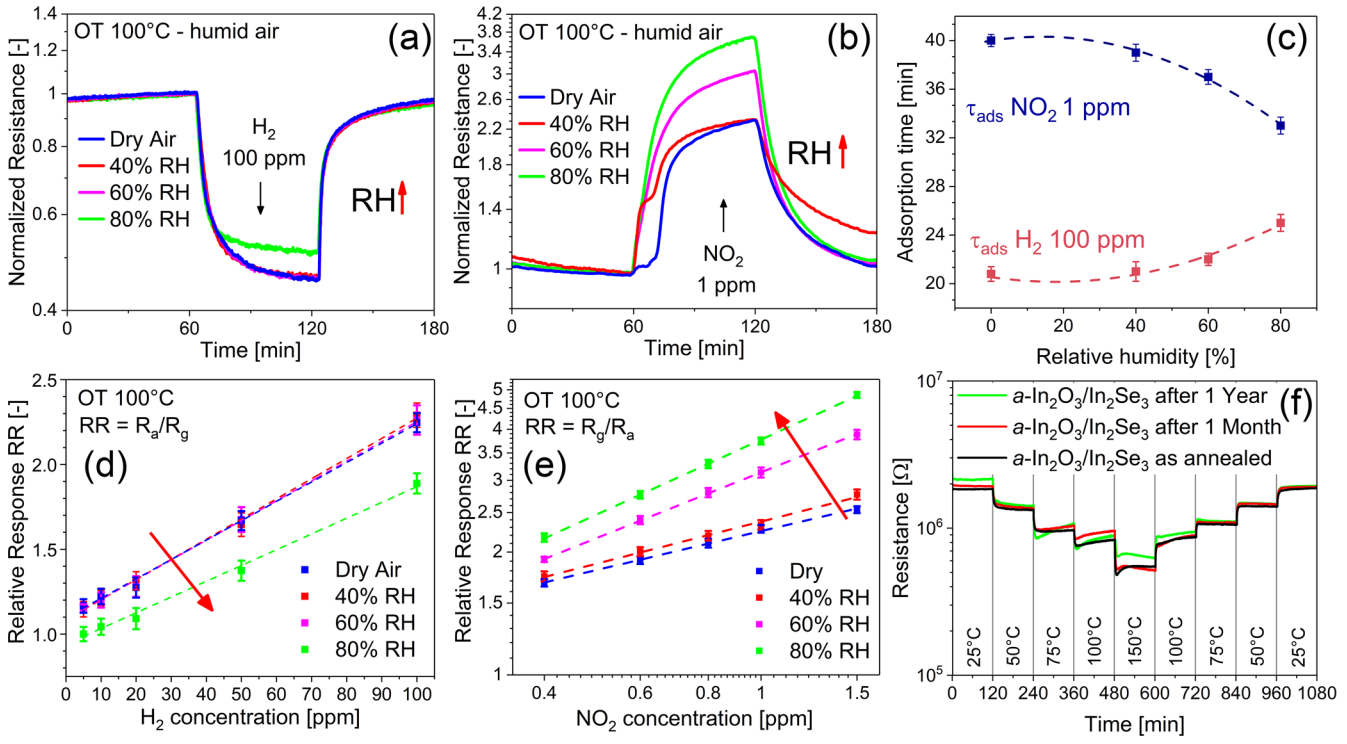

Figure 6. (a,b) Sensor's responses to increasing RH % content (as to the direction of the red arrow) to 100 ppm H_2 and 1 ppm NO_2; (c) adsorption times to 100 and 1 ppm NO_2 as a function of the RH % content; (d,e) log/log calibration plots at 100 °C OT and increasing RH % contents (as to the red arrow) from 0 to 80% (RH at 25 °C) to H_2 and NO_2; (f) BLR variations in dry air at different OTs by increasing/decreasing the OT in the 25−150−25 °C range. Black line: as-annealed *a*-In_2O_3/In_2Se_3; red: measured after 1 month; green: after 1 year of continuous delivery at 100 °C OT. Associated standard deviations $\sigma \pm 0.2$, calculated over a set of five identical measurements.

heterojunction, the increase of the RH % content displays an antisynergistic/synergistic effect upon (i) H_2/NO_2 sensor signal variation and (ii) H_2/NO_2 adsorption times. Overall, the single effect of adsorbing water is to decrease the absolute value of the BLR of the material for all the investigated combinations. Finally, the long-term stability properties of the BLR and sensor's signal (RRs) have been recorded by comparing the electrical signals of the as-annealed *a*-In_2O_3/In_2Se_3 with that of the same sample after 1 month and 1 year of continuous delivery at a 100 °C OT. Notably, excellent reproducibility of the BLR at different OTs between 25 and 150−25 °C is displayed in the dry-air background in Figure 6f. Moreover, the excellent long-term stability for 1 year of both BLR and sensor signals to H_2 and NO_2, at 75 and 100 °C OTs as shown in Figure S7, presents indirect proof that the oxide skin layer effectively passivates the underlying 2D-In_2Se_3 from spontaneous degradation.

Normalizing from literature, we finally compared the experimental LOD, sensor's signal responses (RRs at 10 ppm H_2), and OTs of best-performing materials and structures in Table 2. MO undoubtedly perform better but at the expense of higher OTs. Surprisingly, a very limited number of 2D layered interfaces comprising 2D carbon materials and TMDs/MCs have been found to respond to few ppm H_2 with low LODs. Amorphous/crystalline *a*-MO_x/TMD heterostructures operating at mild OTs (100 °C) show better features as compared to simple 2D TMD/MC interfaces, possibly on account of the role played by the oxide amorphous layer to enhance gas response.

3.4. Discussion. We demonstrated (Figure 1f) that both exfoliation yields and ARs (i.e., the ratio of lateral dimension to the thickness) (Figure 1g,h) depend on the physio-chemical features of the solvent and the sonication/centrifugation process conditions. However, to date, there are no literature investigations demonstrating possible correlations between the AR and the gas sensing response. Conversely, as recently reported, flakes' edges with high concentrations of dangling bonds with respect to terraces, represent the most reacting parts of the nanosheets.[56] These findings address the usefulness of maximizing the length of the exposed edges, with respect to the surface, which enhances the chemical activity of the gas molecules. The passivation strategy to preserve TMDs/MCs from environmental degradation, accounts for controlled oxidation in air of exfoliated In_2Se_3, yielding the formation of an amorphous skin, which guarantees excellent baseline and sensor's signal reproducibility after 1 year of delivery as shown in Figure 6f. Overall, the oxidation mechanism induces an isomorphic conversion of 2D In_2Se_3 into 2D *a*-In_2O_3, thus preserving in the *a*-In_2O_3/In_2Se_3 annealed flakes all the surface-to-volume advantages of the precursor 2D In_2Se_3 layered structure.

The oxidation process of TMDs (MX_2: M = Mo, W, X = S, Se) and MCs (MX: M = Ga, In, Ge, Sn; X = S, Se) in air consists of: (i) the formation of edge and/or basal plane vacancy (i.e., either metal or chalcogen), (ii) the diffusion of molecular oxygen (O_2) inside the material, (iii) the dissociative chemisorption of O_2 as atomic oxygen (O) over the vacancy, and (iv) the annihilation of the vacancy by the formation of metal−oxygen (M−O) bonds.[57] Specifically, it has been theoretically found that the formation of a single selenium vacancy is energetically favorable in the InSe monolayer (~1.9 eV) and that the O_2 dissociation over the Se vacancy is highly

https://doi.org/10.1021/acsanm.3c00380
ACS Appl. Nano Mater. 2023, 6, 6011−6023

exothermic (4.57 eV),[58] leading to the formation of a stable In−O bond. Besides energetics, from a kinetic point of view, it can be possibly assumed that the oxidation process is governed by the diffusion of molecular oxygen (O_2) from the surface of the 2D material to the selenium vacancy sites, following a shrinking-core reaction mechanism,[59] as detailed in Section S4. According to this model, the as-formed *a*-In_2O_3 amorphous skin builds up a diffusion boundary layer which controls the O_2 diffusion toward the unreacted particle core of In_2Se_3. It turns out that the oxidation rate of rectangular stacked nanosheets of In_2Se_3 monolayers depends on the square root of the annealing time and exponentially on the annealing temperature, highlighting the higher significance of annealing temperature with respect to the duration time. Remarkably, the exponential temperature correlation would imply that the oxidation rate of In_2Se_3 is negligible at room temperature (i.e., referred to as spontaneous oxidation), which is apparently in contrast to the 25% of *a*-In_2O_3 phase found by XPS analysis, in the as-exfoliated In_2Se_3 (Figure 3f). Notably, XPS measurements, shown in Figure S4, show that pristine commercial crystals are already oxidized, probably depending on the synthesis route, with approximately the same amount of *a*-In_2O_3 phase content as the as-exfoliated sample. As a consequence, spontaneous oxidation at room temperature under dry/wet environmental laboratory conditions or due to the exfoliation process can be excluded. However, the occurrence of a preoxidized state (i.e., 25% *a*-In_2O_3) in the as-exfoliated samples does not interfere with the thermal oxidation synthesis process at a higher temperature. Moreover, congruent to the kinetic model, by changing the annealing temperature, it is possible to modulate and control the thickness of the skin oxide, although focused experiments are needed to validate the model. In conclusion, annealing at 180 °C for 24 h enhances the formation of an *a*-In_2O_3 skin layer, which kinetically inhibits oxygen diffusion at lower temperatures, therefore effectively passivating the In_2Se_3/In_2O_3 heterostructure from further oxidation. The stabilization of the sensor's BLR for a period of 1 year, at a 100 °C OT (Figure S7), is indirect proof of the effectiveness of the passivation procedure.

The gas sensing response of the *a*-In_2O_3/In_2Se_3 heterostructure behaves like an *n*-type crystalline In_2O_3 chemoresistive H_2/NO_2 sensor.[60] The higher sensor signal amplitude and better detection limits of the *a*-In_2O_3/In_2Se_3 heterostructure with respect to 2D-TMDs/MCs shown in Table 2 account for the presence of Se and O_2 vacancies within the amorphous structure of *a*-In_2O_3[31] which largely improve gas adsorption. According to the literature, following the Kröger−Vink notation, sensor signal variation is driven by redox surface reactions between H_2, NO_2, and H_2O molecules with positively ionized oxygen vacancies ($V_O^{\bullet\bullet}$), ionosorbed oxygen (O_2'), hydroxyls (OH'), rooted $(OH)_O^{\bullet}$, and lattice In_{In}^{X} and Se_{Se}^{X}. All these species compete at the same time with the interfering gases. Specifically, at low OT (T < 130 °C) and dry air, oxygen adsorbs over ($V_O^{\bullet\bullet}$), according to reaction (1), increasing the sensor's resistance

$$O_2 + V_O^{\bullet\bullet} + e' \rightleftarrows (O_2' - V_O^{\bullet\bullet})_{ADS} \quad (1)$$

Following a combustion mechanism, hydrogen reacts with ionosorbed oxygen, releasing a vacancy and an electron, decreasing the sensor's resistance as per reaction (2).

$$2H_2 + (O_2' - V_O^{\bullet\bullet})_{ADS} \rightleftarrows 2H_2O_{(g)} + V_O^{\bullet\bullet} + e' \quad (2)$$

NO_2 gas, conversely, can either react with ($O_2' - V_O^{\bullet\bullet}$) according to reaction (3) (in this case, NO_2, being more electronegative simply displaces adsorbed oxygen, broadening the depletion layer) or directly react with free oxygen vacancies according to reaction (4), forming nitrite species and consuming electrons. In both cases, NO_2 gas increases the sensor's resistance.

$$NO_{2(g)} + (O_2' - V_O^{\bullet\bullet})_{ADS} \rightleftarrows (NO_2' - V_O^{\bullet\bullet})_{ADS} + O_{2(g)} \quad (3)$$

$$NO_{2(g)} + V_O^{\bullet\bullet} + e' \rightleftarrows (NO_2' - V_O^{\bullet\bullet})_{ADS} \quad (4)$$

Water vapor, on the other hand, reacts with sensor's surface mostly in a dissociative chemisorption mode,[15] releasing electrons in the conduction band of the material, according to reactions (5−7)

$$H_2O + 2In_{In}^{X} + (O_2' - V_O^{\bullet\bullet}) \rightleftarrows 2[In_{In}^{\bullet} - OH'] + V_O^{\bullet\bullet} + e' + \frac{1}{2}O_2 \quad (5)$$

$$H_2O + In_{In}^{X} + O_O^{X} \rightleftarrows [In_{In}^{\bullet} - OH'] + (OH)_O^{\bullet} + e' \quad (6)$$

$$H_2O + 2In_{In}^{X} + O_O^{X} \rightleftarrows 2[In_{In}^{\bullet} - OH'] + V_O^{\bullet\bullet} + 2e' \quad (7)$$

In the first mechanism (5) proposed by Heinrich and Cox,[61] water vapor displaces adsorbed oxygen, forming hydroxyls (OH') and releasing a vacancy ($V_O^{\bullet\bullet}$) and e′. This mechanism seems to be supported by a strong reduction of the $O_2'/OH^{\bullet}$ radicals' ratio in humid conditions, as recorded by EPR measurements for crystalline SnO_2.[62] In the second mechanism, proposed by Heiland and Kohl[63] (6,7), either rooted $(OH)_O^{\bullet}$ or two terminal (OH') groups and an oxygen vacancy are formed. All these mechanisms, producing electrons, are congruent with the decrease of the BLR in 40% RH as recorded in Figure 5g,h. Remarkably, as shown in Figure 6a,d, increasing the humidity content decreases the H_2 sensor's signal amplitude, following the same response as to CO in SnO_2 and In_2O_3 crystalline MOs.[64−66] Combining these observations, the decrease of the H_2 sensor signal with increasing humidity, accounts first for the synergistic action of reactions (2, 5−7) which release electrons/vacancies (leading to a resistance decrease), followed by the recombination of air oxygen with the as-formed electrons/vacancies, as for reaction (1) (leading to a resistance increase). An equilibrium is established, where a resistance decrease is partially mitigated by a resistance increase. Overall, humidity negatively affects sensor's signal amplitude to H_2, according to an antisynergistic effect. Conversely, increasing humidity increases the NO_2 sensor signal, as shown in Figure 6b,e. Specifically, in dry air, NO_2 depletes electrons from the conduction band, increasing the resistance according to reaction (4); meanwhile, humid air releases vacancies and electrons, as to reactions (5−7). Considering now that NO_2 gas has a stronger oxidizing activity than oxygen (its electron affinity E_{ea} (NO_2) = 2.27 eV is higher than E_{ea} (O_2) = 0.44 eV), in NO_2 atmosphere, reaction (4) will prevail with respect to the reoxidation of the surface operated by air-oxygen (1). Combining these observations, the resistance increase due to the NO_2 reaction (4) in dry air (resistance increases) is boosted, in humid air, by further NO_2 reaction with electrons/vacancies released by water adsorption (5−7) (resistance increase). Overall humidity

https://doi.org/10.1021/acsanm.3c00380
ACS Appl. Nano Mater. 2023, 6, 6011−6023

positively affects sensor's signal increase to NO_2 according to a synergistic effect. Interestingly, operando DRIFTS investigations over crystalline In_2O_3[67] at 130 °C pointed out that hydroxyl groups formed by water vapor adsorption (5) can be easily displaced by NO_2 adsorption, according to a "wet" adsorption mechanism, as to reaction (8). This mechanism, as previously reported,[61] clearly accounts for the NO_2 gas sensor signal increase with increasing water vapor content, at low temperatures (T < 130 °C)

$$NO_2 + [In_{In}^{\bullet} - OH'] + (OH)_O^{\bullet} + 2e' \rightleftarrows [In_{In}^{\bullet} - NO_2'] + H_2O + O_O' \quad (8)$$

The increase/decrease of the H_2/NO_2 adsorption times with increasing humidity content, as shown in Figure 6c, is finally explained considering that H_2 gas reacts with only $(O_2' - V_O^{\bullet\bullet})$ (2), whereas NO_2 reacts with $(O_2' - V_O^{\bullet\bullet})$, $V_O^{\bullet\bullet}$and OH′ (3, 4, 8). In a H_2 atmosphere, increasing the humidity content decreases the concentration of $(O_2' - V_O^{\bullet\bullet})$ due to the competitive action of H_2 and H_2O over the same adsorption site [reactions (2) and (5)]. In this case, H_2 adsorption time increases with increasing humidity content. Conversely, the increase of the concentration of $V_O^{\bullet\bullet}$ and OH′ adsorption sites with increasing humidity content [reactions (5,6,7)] increases the number of available adsorption sites for NO_2, therefore, decreasing adsorption time. It should be noted that, according to a previously reported mechanism,[68] all the above-mentioned reactions tune the extension of the depletion layers (known as the Debye length) within the a-In_2O_3 oxide skin. With an associated a-In_2O_3 skin thickness of 5−7 nm (see Figure 3e), considering a Debye length between 5 and 50 nm, it is reasonable that the a-In_2O_3 oxide skin is fully or partially depleted of electrons when in contact with oxidizing gas [NO_2—reactions (3, 4, 8)] or reducing [H_2, H_2O—reactions (2, 5−7)] gases, respectively. Assuming a parallel contribution scheme of the a-In_2O_3 skin and In_2Se_3 bulk to the conduction model of the whole flake,[68] taking into consideration that atomically thin layers of In_2O_3 exhibit 2 orders-of-magnitude enhancement of conductivity and mobility with respect to few-layer In_2Se_3,[69] we may conclude that the outer a-In_2O_3 shell governs the conduction mechanism of the whole flake. This is achieved, depending on the nature of the adsorbing gas, by the modulation of the Debye length within the a-In_2O_3 skin. Lastly, flake-to-flake contacts between loosely stacked flakes built up, as previously depicted,[70] Schottky barriers between the flakes, modulating the conductivity similarly to the conduction mechanism of unsintered MO nanoparticles in traditional chemoresistive sensors.

4. CONCLUSIONS

We have reported a simple thermal treatment process in air, carried out at temperatures below the recrystallization temperature of the native oxide that induces the formation of ∼5−7 nm thin, amorphous oxide layers over liquid-phase exfoliated (∼25−30 nm thick) 2D-In_2Se_3 flakes, leading to the formation of an amorphous/crystalline a-In_2O_3/In_2Se_3 heterostructure. We found that the self-assembled growth of the native oxide leads to an isomorphic conversion of 2D-In_2Se_3 into a-In_2O_3, implicating that the layered shape of the precursor 2D-In_2Se_3 exfoliated is fully maintained. We also found that the a-In_2O_3/In_2Se_3 heterostructure responds to H_2 and NO_2 gases with associated detection limits as low as 5 ppm and RR (R_a/R_g) = 1.2 to 10 ppm H_2, the highest with respect to only exfoliated 2D TMD/MC sensors. Most strikingly, the a-In_2O_3 skin oxide effectively passivates the underlying 2D-In_2Se_3 from further ambient oxidation, as attested by the excellent long-term reproducibility of the BLR and sensor's signal to H_2 and NO_2, over 1 year delivery at 100 °C OT. We finally studied a possible gas sensing mechanism which accounts for a synergistic/antisynergistic effect played by humid water over the H_2/NO_2 sensor signal amplitude and adsorption times. In conclusion, this methodology, which can be successfully extended to a large variety of TMDs and MCs, represents a possible strategy to improve the long-term stability of the electrical properties of TMDs/MCs devices for gas sensing applications.

■ ASSOCIATED CONTENT

Supporting Information

The Supporting Information is available free of charge at https://pubs.acs.org/doi/10.1021/acsanm.3c00380.

Experimental section, Rhodiasolv RPDE's FTIR characterization, microstructural characterization, shrinking-core model of In_2Se_3 oxidation, and gas sensing responses (PDF)

■ AUTHOR INFORMATION

Corresponding Author

Vittorio Ricci − *Department of Industrial and Information Engineering and Economics, University of L'Aquila, I-67100 L'Aquila, Italy;* orcid.org/0000-0002-6230-4128; Email: vittorio.ricci@gradaute.univaq.it

Authors

Valentina Paolucci − *Department of Industrial and Information Engineering and Economics, University of L'Aquila, I-67100 L'Aquila, Italy; UdR INSTM of L'Aquila, I-67100 L'Aquila, Italy;* orcid.org/0000-0003-0641-7926

Jessica De Santis − *Department of Industrial and Information Engineering and Economics, University of L'Aquila, I-67100 L'Aquila, Italy; UdR INSTM of L'Aquila, I-67100 L'Aquila, Italy*

Luca Lozzi − *Department of Physical and Chemical Sciences, University of L'Aquila, 67100 L'Aquila (AQ), Italy*

Carlo Cantalini − *Department of Industrial and Information Engineering and Economics, University of L'Aquila, I-67100 L'Aquila, Italy; UdR INSTM of L'Aquila, I-67100 L'Aquila, Italy*

Complete contact information is available at: https://pubs.acs.org/10.1021/acsanm.3c00380

Author Contributions

Author Credit statement: V.P. performed all material synthesis, conducted the research investigation process, evaluated the measurements, and drafted the manuscript. J.D.S. performed material characterization and conducted a formal analysis of the collected data by the application of dedicated software. V.R. performed material synthesis and electrical characterization addressing a model of the oxidation mechanism of In_2Se_3. L.L. carried out the research and investigation process by performing XPS experiments. C.C. addressed the goals of the research, supervised and coordinated experiments, and finalized the manuscript.

https://doi.org/10.1021/acsanm.3c00380
ACS Appl. Nano Mater. 2023, 6, 6011−6023

Notes

The authors declare no competing financial interest.

■ ACKNOWLEDGMENTS

TEM experiments at Jožef Stefan Institute-Ljubljana were carried out within the framework of the GAS-HYBRID-TMDS proposal within the ESTEEM3 grant agreement no. 823717.

■ REFERENCES

(1) EPA. Primary National Ambient Air Quality Standards (NAAQS) for Nitrogen Dioxide https://www.epa.gov/no2-pollution/primary-national-ambient-air-quality-standards-naaqs-nitrogen-dioxide (accessed Feb 27, 2023).
(2) Shi, Y.; Xu, H.; Liu, T.; Zeb, S.; Nie, Y.; Zhao, Y.; Qin, C.; Jiang, X. Advanced Development of Metal Oxide Nanomaterials for H_2 Gas Sensing Applications. *Adv. Mater.* **2021**, *2*, 1530−1569.
(3) Tyagi, S.; Chaudhary, M.; Ambedkar, A. K.; Sharma, K.; Gautam, Y. K.; Singh, B. P. Metal Oxide Nanomaterial-Based Sensors for Monitoring Environmental NO_2 and Its Impact on the Plant Ecosystem: A Review. *Sens. Diagn.* **2022**, *1*, 106−129.
(4) Meng, Z.; Stolz, R. M.; Mendecki, L.; Mirica, K. A. Electrically-Transduced Chemical Sensors Based on Two-Dimensional Nanomaterials. *Chem. Rev.* **2019**, *119*, 478−598.
(5) Zhou, T.; Zhang, T. Recent Progress of Nanostructured Sensing Materials from 0D to 3D: Overview of Structure−Property-Application Relationship for Gas Sensors. *Small Methods* **2021**, *5*, 2100515.
(6) Wu, R.; Xin, T.; Wang, Y.; Wang, T.; Liu, L.; Hao, J. A Lateral Built-in Field of the 2D/2D $SnS_2/SnSe_2$ in-Plane Heterostructure with Boosted Interfacial Charge Transfer. *J. Mater. Chem. A* **2022**, *10*, 14810−14819.
(7) Boukhvalov, D. W.; Paolucci, V.; D'Olimpio, G.; Cantalini, C.; Politano, A. Chemical Reactions on Surfaces for Applications in Catalysis, Gas Sensing, Adsorption-Assisted Desalination and Li-Ion Batteries: Opportunities and Challenges for Surface Science. *Phys. Chem. Chem. Phys.* **2021**, *23*, 7541−7552.
(8) Paolucci, V.; D'Olimpio, G.; Kuo, C. N.; Lue, C. S.; Boukhvalov, D. W.; Cantalini, C.; Politano, A. Self-Assembled $SnO_2/SnSe_2$ Heterostructures: A Suitable Platform for Ultrasensitive NO_2 and H_2 Sensing. *ACS Appl. Mater. Interfaces* **2020**, *12*, 34362−34369.
(9) Li, Q.; Zhou, Q.; Shi, L.; Chen, Q.; Wang, J. Recent Advances in Oxidation and Degradation Mechanisms of Ultrathin 2D Materials under Ambient Conditions and Their Passivation Strategies. *J. Mater. Chem. A* **2019**, *7*, 4291−4312.
(10) Shi, L.; Zhou, Q.; Zhao, Y.; Ouyang, Y.; Ling, C.; Li, Q.; Wang, J. Oxidation Mechanism and Protection Strategy of Ultrathin Indium Selenide: Insight from Theory. *J. Phys. Chem. Lett.* **2017**, *8*, 4368−4373.
(11) Hong, T. J.; Chen, Y. X.; Quyen, N. N.; Chen, Y. H.; Chen, C. H.; Huang, B. H.; Chen, J. Y.; Ho, M. S.; Juang, J. Y.; Chen, C. H.; Luo, C. W. Snapshots of Ambient Aging in 2D-Layered GaSe. *ACS Appl. Electron. Mater.* **2022**, *4*, 3049−3055.
(12) Boukhvalov, D. W.; Nappini, S.; Vorokhta, M.; Menteş, T. O.; Piliai, L.; Panahi, M.; Genuzio, F.; De Santis, J.; Kuo, C. N.; Lue, C. S.; Paolucci, V.; Locatelli, A.; Bondino, F.; Politano, A. Revisiting the Chemical Stability of Germanium Selenide (GeSe) and the Origin of Its Photocatalytic Efficiency. *Adv. Funct. Mater.* **2021**, *31*, 2106228.
(13) Zhang, B.; Li, A.; Han, G.; Zhang, Z.; Peng, K.; Gong, X.; Zhou, X.; Han, X. Dynamic Epitaxial Crystallization of $SnSe_2$ on the Oxidized SnSe Surface and Its Atomistic Mechanisms. *ACS Appl. Mater. Interfaces* **2020**, *12*, 27700−27707.
(14) Paolucci, V.; De Santis, J.; Lozzi, L.; Giorgi, G.; Cantalini, C. Layered Amorphous a-SnO_2 Gas Sensors by Controlled Oxidation of 2D-$SnSe_2$. *Sens. Actuators, B* **2022**, *350*, 130890.
(15) Paolucci, V.; De Santis, J.; Ricci, V.; Lozzi, L.; Giorgi, G.; Cantalini, C. Bidimensional Engineered Amorphous *a*-SnO_2 Interfaces: Synthesis and Gas Sensing Response to H_2S and Humidity. *ACS Sens.* **2022**, *7*, 2058−2068.
(16) Vidal, T.; Bramati, V.; Murthy, K.; Abribat, B.; Devisetty, B.; Dean, S. W. A New Environmentally Friendly Solvent of Low Toxicity for Crop Protection Formulations. *ASTM Spec. Tech. Publ.* **2011**, *8*, 103716.
(17) Solvay Novecare. *Rhodiasolv RPDE SDS*. http://208.112.58.204/pridesol/documents/sds/Dibasic-Ester-Solvay-2014-12-10.pdf.
(18) Hernandez, Y.; Nicolosi, V.; Lotya, M.; Blighe, F. M.; Sun, Z.; De, S.; McGovern, I. T.; Holland, B.; Byrne, M.; Gun'Ko, Y. K.; Boland, J. J.; Niraj, P.; Duesberg, G.; Krishnamurthy, S.; Goodhue, R.; Hutchison, J.; Scardaci, V.; Ferrari, A. C.; Coleman, J. N. High-Yield Production of Graphene by Liquid-Phase Exfoliation of Graphite. *Nat. Nanotechnol.* **2008**, *3*, 563−568.
(19) Paolucci, V.; D'Olimpio, G.; Lozzi, L.; Mio, A. M.; Ottaviano, L.; Nardone, M.; Nicotra, G.; Le-Cornec, P.; Cantalini, C.; Politano, A. Sustainable Liquid-Phase Exfoliation of Layered Materials with Nontoxic Polarclean Solvent. *ACS Sustainable Chem. Eng.* **2020**, *8*, 18830−18840.
(20) Shen, J.; Wu, J.; Wang, M.; Dong, P.; Xu, J.; Li, X.; Zhang, X.; Yuan, J.; Wang, X.; Ye, M.; Vajtai, R.; Lou, J.; Ajayan, P. M. Surface Tension Components Based Selection of Cosolvents for Efficient Liquid Phase Exfoliation of 2D Materials. *Small* **2016**, *12*, 2741−2749.
(21) Nian, T.; Wang, Z.; Dong, B. Thermoelectric properties of *α*-In2Se3 monolayer. *Appl. Phys. Lett.* **2021**, *118*, 033103.
(22) Randová, A.; Bartovská, L.; Morávek, P.; Matějka, P.; Novotná, M.; Matějková, S.; Drioli, E.; Figoli, A.; Lanč, M.; Friess, K. A Fundamental Study of the Physicochemical Properties of RhodiasolvPolarclean: A Promising Alternative to Common and Hazardous Solvents. *J. Mol. Liq.* **2016**, *224*, 1163−1171.
(23) Halonen, S.; Kangas, T.; Haataja, M.; Lassi, U. Urea-Water-Solution Properties: Density, Viscosity, and Surface Tension in an Under-Saturated Solution. *Emiss. Control Sci. Technol.* **2017**, *3*, 161−170.
(24) Cunningham, G.; Lotya, M.; Cucinotta, C. S.; Sanvito, S.; Bergin, S. D.; Menzel, R.; Shaffer, M. S. P.; Coleman, J. N. Solvent Exfoliation of Transition Metal Dichalcogenides: Dispersibility of Exfoliated Nanosheets Varies Only Weakly between Compounds. *ACS Nano* **2012**, *6*, 3468−3480.
(25) Lyklema, J. The Surface Tension of Pure Liquids: Thermodynamic Components and Corresponding States. *Colloids Surf., A* **1999**, *156*, 413−421.
(26) Coleman, J. N.; Lotya, M.; O'Neill, A.; Bergin, S. D.; King, P. J.; Khan, U.; Young, K.; Gaucher, A.; De, S.; Smith, R. J.; Shvets, I. V.; Arora, S. K.; Stanton, G.; Kim, H. Y.; Lee, K.; Kim, G. T.; Duesberg, G. S.; Hallam, T.; Boland, J. J.; Wang, J. J.; Donegan, J. F.; Grunlan, J. C.; Moriarty, G.; Shmeliov, A.; Nicholls, R. J.; Perkins, J. M.; Grieveson, E. M.; Theuwissen, K.; McComb, D. W.; Nellist, P. D.; Nicolosi, V. Two-Dimensional Nanosheets Produced by Liquid Exfoliation of Layered Materials. *Science* **2011**, *331*, 568−571.
(27) Zappia, M. I.; Bianca, G.; Bellani, S.; Serri, M.; Najafi, L.; Oropesa-Nuñez, R.; Martín-García, B.; Bouša, D.; Sedmidubský, D.; Pellegrini, V.; Sofer, Z.; Cupolillo, A.; Bonaccorso, F. Solution-Processed GaSe Nanoflake-Based Films for Photoelectrochemical Water Splitting and Photoelectrochemical-Type Photodetectors. *Adv. Funct. Mater.* **2020**, *30*, 1909572.
(28) Küpers, M.; Konze, P. M.; Meledin, A.; Mayer, J.; Englert, U.; Wuttig, M.; Dronskowski, R. Controlled Crystal Growth of Indium Selenide, In_2Se_3, and the Crystal Structures of α-In_2Se_3. *Inorg. Chem.* **2018**, *57*, 11775−11781.
(29) Perrozzi, F.; Emamjomeh, S. M.; Paolucci, V.; Taglieri, G.; Ottaviano, L.; Cantalini, C. Thermal Stability of WS_2 Flakes and Gas Sensing Properties of WS_2/WO_3 Composite to H_2, NH_3 and NO_2. *Sens. Actuators, B* **2017**, *243*, 812−822.
(30) Popović, S.; Tonejc, A.; Gržeta-Plenković, B.; Čelustka, B.; Trojko, R. Revised and New Crystal Data for Indium Selenides. *J. Appl. Crystallogr.* **1979**, *12*, 416−420.
(31) Ho, C. H.; Lin, C. H.; Wang, Y. P.; Chen, Y. C.; Chen, S. H.; Huang, Y. S. Surface Oxide Effect on Optical Sensing and

https://doi.org/10.1021/acsanm.3c00380
ACS Appl. Nano Mater. 2023, 6, 6011−6023

Photoelectric Conversion of α-In_2Se_3 Hexagonal Microplates. *ACS Appl. Mater. Interfaces* **2013**, *5*, 2269−2277.
(32) Liu, W. K.; Yuen, W. T.; Stradling, R. A. Preparation of InSb Substrates for Molecular Beam Epitaxy. *J. Vac. Sci. Technol., B: Microelectron. Nanometer Struct.–Process., Meas., Phenom.* **1995**, *13*, 1539−1545.
(33) Wei, W.; Wei, Z.; Li, R.; Li, Z.; Shi, R.; Ouyang, S.; Qi, Y.; Philips, D. L.; Yuan, H. Subsurface Oxygen Defects Electronically Interacting with Active Sites on In_2O_3 for Enhanced Photothermocatalytic CO_2 Reduction. *Nat. Commun.* **2022**, *13*, 1−12.
(34) Shan, F.; Sun, H. Z.; Lee, J. Y.; Pyo, S.; Kim, S. J. Improved High-Performance Solution Processed In_2O_3 Thin Film Transistor Fabricated by Femtosecond Laser Pre-Annealing Process. *IEEE Access* **2021**, *9*, 44453−44462.
(35) Quereda, J.; Biele, R.; Rubio-Bollinger, G.; Agraït, N.; D'Agosta, R.; Castellanos-Gomez, A. Strong Quantum Confinement Effect in the Optical Properties of Ultrathin α-In_2Se_3. *Adv. Opt. Mater.* **2016**, *4*, 1939−1943.
(36) Waghmare, A.; Sharma, V.; Shinde, P.; Punde, A.; Vairale, P.; Hase, Y.; Pandharkar, S.; Nair, S.; Aher, R.; Doiphode, V.; Shah, S.; Rahane, S.; Bade, B.; Prasad, M.; Rondiya, S.; Jadkar, S. Preparation and Characterization of γ-In_2Se_3 Thin-Film Photoanodes for Photoelectrochemical Water Splitting. *J. Solid State Electrochem.* **2022**, *26*, 219−232.
(37) Wang, C.; Li, Y. D.; Wang, J. W.; Deng, Z. X.; Wang, R. J.; Fan, S. S. Solvothermal Processes to Indium Selenide Precursors and Their Conversion to Phase-Pure Polycrystalline In_2Se_3. *Main Group Met. Chem.* **2001**, *24*, 21−26.
(38) Zhu, C.; Shen, H.; Liu, H.; Lv, X.; Li, Z.; Yuan, Q. Solution-Processable Two-Dimensional In_2Se_3 Nanosheets as Efficient Photothermal Agents for Elimination of Bacteria. *Chem.—Eur. J.* **2018**, *24*, 19060−19065.
(39) Kubelka, P.; Munk, F. An Article on Optics of Paint Layers. *Z. Tech. Phys.* **1931**, *12*, 593.
(40) Makuła, P.; Pacia, M.; Macyk, W. How To Correctly Determine the Band Gap Energy of Modified Semiconductor Photocatalysts Based on UV-Vis Spectra. *J. Phys. Chem. Lett.* **2018**, *9*, 6814−6817.
(41) Beji, N.; Souli, M.; Ajili, M.; Azzaza, S.; Alleg, S.; Turki, N. K. Effect of Iron Doping on Structural, Optical and Electrical Properties of Sprayed In_2O_3 Thin Films. *Superlattices Microstruct.* **2015**, *81*, 114−128.
(42) Perkins, F. K.; Friedman, A. L.; Cobas, E.; Campbell, P. M.; Jernigan, G. G.; Jonker, B. T. Chemical Vapor Sensing with Monolayer MoS_2. *Nano Lett.* **2013**, *13*, 668−673.
(43) Li, Z.; Yan, S.; Wu, Z.; Li, H.; Wang, J.; Shen, W.; Wang, Z.; Fu, Y. Q. Hydrogen Gas Sensor Based on Mesoporous In_2O_3 with Fast Response/Recovery and Ppb Level Detection Limit. *Int. J. Hydrogen Energy* **2018**, *43*, 22746−22755.
(44) Chava, C.; Oh, S. Y.; Yu, Y. T. Enhanced H_2 Gas Sensing Properties of Au@In_2O_3 Core-Shell Hybrid Metal-Semiconductor Heteronanostructures. *CrystEngComm* **2016**, *18*, 3655−3666.
(45) Wang, Y.; Zhao, Z.; Sun, Y.; Li, P.; Ji, J.; Chen, Y.; Zhang, W.; Hu, J. Fabrication and Gas Sensing Properties of Au-Loaded SnO_2 Composite Nanoparticles for Highly Sensitive Hydrogen Detection. *Sens. Actuators, B* **2017**, *240*, 664−673.
(46) Wang, F.; Hu, K.; Liu, H.; Zhao, Q.; Wang, K.; Zhang, Y. Low Temperature and Fast Response Hydrogen Gas Sensor with Pd Coated SnO_2 Nanofiber Rods. *Int. J. Hydrogen Energy* **2020**, *45*, 7234−7242.
(47) Hu, J.; Sun, Y.; Xue, Y.; Zhang, M.; Li, P.; Lian, K.; Zhuiykov, S.; Zhang, W.; Chen, Y. Highly Sensitive and Ultra-Fast Gas Sensor Based on CeO_2-Loaded In_2O_3 Hollow Spheres for Ppb-Level Hydrogen Detection. *Sens. Actuators, B* **2018**, *257*, 124−135.
(48) Lee, J. H.; Kim, J. Y.; Mirzaei, A.; Kim, H. W.; Kim, S. S. Significant Enhancement of Hydrogen-Sensing Properties of ZnO Nanofibers through NiO Loading. *Nanomaterials* **2018**, *8*, 902.
(49) Shin, D. H.; Lee, J. S.; Jun, J.; An, J. H.; Kim, S. G.; Cho, K. H.; Jang, J. Flower-like Palladium Nanoclusters Decorated Graphene Electrodes for Ultrasensitive and Flexible Hydrogen Gas Sensing. *Sci. Rep.* **2015**, *5*, 1−11.
(50) Lee, J. S.; Oh, J.; Jun, J.; Jang, J. Wireless Hydrogen Smart Sensor Based on Pt/Graphene-Immobilized Radio-Frequency Identification Tag. *ACS Nano* **2015**, *9*, 7783−7790.
(51) Zhang, Z.; Zou, X.; Xu, L.; Liao, L.; Liu, W.; Ho, J.; Xiao, X.; Jiang, C.; Li, J. Hydrogen Gas Sensor Based on Metal Oxide Nanoparticles Decorated Graphene Transistor. *Nanoscale* **2015**, *7*, 10078−10084.
(52) Gottam, S. R.; Tsai, C. T.; Wang, L. W.; Wang, C. T.; Lin, C. C.; Chu, S. Y. Highly Sensitive Hydrogen Gas Sensor Based on a MoS_2-Pt Nanoparticle Composite. *Appl. Surf. Sci.* **2020**, *506*, 144981.
(53) Kathiravan, D.; Huang, B. R.; Saravanan, A.; Prasannan, A.; Hong, P. Da. Highly Enhanced Hydrogen Sensing Properties of Sericin-Induced Exfoliated MoS_2 Nanosheets at Room Temperature. *Sens. Actuators, B* **2019**, *279*, 138−147.
(54) Zhang, D.; Sun, Y.; Jiang, C.; Zhang, Y. Room Temperature Hydrogen Gas Sensor Based on Palladium Decorated Tin Oxide/Molybdenum Disulfide Ternary Hybrid via Hydrothermal Route. *Sens. Actuators, B* **2017**, *242*, 15−24.
(55) Baek, D. H.; Kim, J. MoS2 Gas Sensor Functionalized by Pd for the Detection of Hydrogen. *Sens. Actuators, B* **2017**, *250*, 686−691.
(56) Agrawal, A. V.; Kumar, R.; Venkatesan, S.; Zakhidov, A.; Zhu, Z.; Bao, J.; Kumar, M.; Kumar, M. Fast Detection and Low Power Hydrogen Sensor Using Edge-Oriented Vertically Aligned 3-D Network of MoS_2 Flakes at Room Temperature. *Appl. Phys. Lett.* **2017**, *111*, 093102.
(57) Longo, R. C.; Addou, R.; Kc, K. C.; Noh, J. Y.; Smyth, C. M.; Barrera, D.; Zhang, C.; Hsu, J. W. P.; Wallace, R. M.; Cho, K. Intrinsic Air Stability Mechanisms of Two-Dimensional Transition Metal Dichalcogenide Surfaces: Basal versus Edge Oxidation. *2D Mater.* **2017**, *4*, 025050.
(58) Ma, D.; Li, T.; Yuan, D.; He, C.; Lu, Z.; Lu, Z.; Yang, Z.; Wang, Y. The Role of the Intrinsic Se and In Vacancies in the Interaction of O_2 and H_2O Molecules with the InSe Monolayer. *Appl. Surf. Sci.* **2018**, *434*, 215−227.
(59) Levenspiel, O. *Chemical Reaction Engineering*, 3rd ed.; John Wiley & Sons, 1999; Chapter 25.
(60) Roso, S.; Bittencourt, C.; Umek, P.; González, O.; Güell, F.; Urakawa, A.; Llobet, E. Synthesis of Single Crystalline In_2O_3 Octahedra for the Selective Detection of NO_2 and H_2 at Trace Levels. *J. Mater. Chem. C* **2016**, *4*, 9418−9427.
(61) Henrich, V. A.; Cox, P. A. Molecular Adsorption on Oxides. *The Surface Science of Metal Oxides*; Cambridge University Press: Cambridge (U.K.), 1994; pp 247−370.
(62) Nasriddinov, A.; Rumyantseva, M.; Konstantinova, E.; Marikutsa, A.; Tokarev, S.; Yaltseva, P.; Fedorova, O.; Gaskov, A. Effect of Humidity on Light-Activated NO and NO_2 Gas Sensing by Hybrid Materials. *Nanomaterials* **2020**, *10*, 915.
(63) Heiland, G.; Kohl, D. Physical and Chemical Aspects of Oxidic Semiconductor Gas Sensors. *Chem. Sens. Technol.* **1988**, *1*, 15−38.
(64) Degler, D.; Junker, B.; Allmendinger, F.; Weimar, U.; Barsan, N. Investigations on the Temperature-Dependent Interaction of Water Vapor with Tin Dioxide and Its Implications on Gas Sensing. *ACS Sens.* **2020**, *5*, 3207−3216.
(65) Boehme, I.; Weimar, U.; Barsan, N. Unraveling the Surface Chemistry of CO Sensing with In_2O_3 Based Gas Sensors. *Sens. Actuators, B* **2021**, *326*, 129004.
(66) Staerz, A.; Weimar, U.; Barsan, N. Current State of Knowledge on the Metal Oxide Based Gas Sensing Mechanism. *Sens. Actuators, B* **2022**, *358*, 131531.
(67) Roso, S.; Degler, D.; Llobet, E.; Barsan, N.; Urakawa, A. Temperature-Dependent NO_2 Sensing Mechanisms over Indium Oxide. *ACS Sens.* **2017**, *2*, 1272−1277.
(68) Barsan, N.; Simion, C.; Heine, T.; Pokhrel, S.; Weimar, U. Modeling of Sensing and Transduction for P-Type Semiconducting Metal Oxide Based Gas Sensors. *J. Electroceram.* **2010**, *25*, 11−19.
(69) Mukherjee, S.; Dutta, D.; Mohapatra, P. K.; Dezanashvili, L.; Ismach, A.; Koren, E. Scalable Integration of Coplanar Heterojunction

https://doi.org/10.1021/acsanm.3c00380
ACS Appl. Nano Mater. 2023, 6, 6011−6023

Monolithic Devices on Two-Dimensional In_2Se_3. *ACS Nano* **2020**, *14*, 17543−17553.
(70) Kelly, A. G.; O'Suilleabhain, D.; Gabbett, C.; Coleman, J. N. The Electrical Conductivity of Solution-Processed Nanosheet Networks. *Nat. Rev. Mater.* **2022**, *7*, 217−234.

https://doi.org/10.1021/acsanm.3c00380
ACS Appl. Nano Mater. 2023, 6, 6011−6023